

# ADVANCED HEALTHCARE MATERIALS



# Wireless, Skin-Interfaced Devices for Pediatric Critical Care: Application to Continuous, Noninvasive Blood Pressure Monitoring

Claire Liu, Jin-Tae Kim, Sung Soo Kwak, Aurelie Hourlier-Fargette, Raudel Avila, Jamie Vogl, Andreas Tzavelis, Ha Uk Chung, Jong Yoon Lee, Dong Hyun Kim, Dennis Ryu, Kelsey B. Fields, Joanna L. Ciatti, Shupeng Li, Masahiro Irie, Allison Bradley, Avani Shukla, Jairo Chavez, Emma C. Dunne, Seung Sik Kim, Jungwoo Kim, Jun Bin Park, Han Heul Jo, Joohee Kim, Michael C. Johnson, Jean Won Kwak, Surabhi R. Madhvapathy, Shuai Xu, Casey M. Rand, Lauren E. Marsillio, Sue J. Hong, Yonggang Huang,\* Debra E. Weese-Mayer,\* and John A. Rogers\*

Indwelling arterial lines, the clinical gold standard for continuous blood pressure (BP) monitoring in the pediatric intensive care unit (PICU), have significant drawbacks due to their invasive nature, ischemic risk, and impediment to natural body movement. A noninvasive, wireless, and accurate alternative would greatly improve the quality of patient care. Recently introduced classes of wireless, skin-interfaced devices offer capabilities in continuous, precise monitoring of physiologic waveforms and vital signs in pediatric and neonatal patients, but have not yet been employed for continuous tracking of systolic and diastolic BP—critical for guiding clinical decision-making in the PICU. The results presented here focus on materials and mechanics that optimize the system-level properties of these devices to enhance their reliable use in this context, achieving full compatibility with the range of body sizes, skin types, and sterilization schemes typically encountered in the PICU. Systematic analysis of the data from these devices on 23 pediatric patients, yields derived, noninvasive BP values that can be quantitatively validated against direct recordings from arterial lines. The results from this diverse cohort, including those under pharmacological protocols, suggest that wireless, skin-interfaced devices can, in certain circumstances of practical utility, accurately and continuously monitor BP in the PICU patient population.

## 1. Introduction

Invasive arterial catheterization with an indwelling arterial line (a-line) forms the basis for continuous blood pressure (BP) monitoring of patients in critical care. These data are extremely important, as highly hypertensive or hypotensive events may indicate dramatic, life-threatening changes in physiological well-being that require medical intervention.<sup>[1–3]</sup> Despite serving as the clinical gold standard for tracking such events, a-lines—received by  $\approx 36\%$  of all adult intensive care unit (ICU) patients in the United States—involve multiple risks, notably limb ischemia and infection.<sup>[2,4–8]</sup> The placement of an a-line also poses its own challenges, including the need for procedural sedation and difficulties in obtaining vascular access in small or very ill patients. These considerations are particularly pronounced in infants admitted to the pediatric ICU (PICU), where intrusive a-lines are disproportionately sized with respect to their small arteries.<sup>[9–11]</sup> Managing such complications requires various

C. Liu, Dr. J.-T. Kim, Dr. S. S. Kwak, Dr. A. Hourlier-Fargette, A. Tzavelis, Dr. H. U. Chung, J. Y. Lee, J. L. Ciatti, M. Irie, J. Kim, J. W. Kwak, S. R. Madhvapathy, Dr. S. Xu, Prof. Y. Huang, Prof. J. A. Rogers  
Querrey Simpson Institute for Bioelectronics  
Northwestern University  
Evanston, IL 60208, USA  
E-mail: y-huang@northwestern.edu; jrogers@northwestern.edu

C. Liu, A. Tzavelis, M. C. Johnson, Dr. S. Xu, Prof. J. A. Rogers  
Department of Biomedical Engineering  
Northwestern University  
Evanston, IL 60208, USA  
Dr. S. S. Kwak  
School of Advanced Materials Science and Engineering  
Sungkyunkwan University (SKKU)  
Suwon 16419, Republic of Korea  
Dr. A. Hourlier-Fargette  
Université de Strasbourg  
CNRS  
Institut Charles Sadron  
Strasbourg F-67000, France

The ORCID identification number(s) for the author(s) of this article can be found under <https://doi.org/10.1002/adhm.202100383>

DOI: 10.1002/adhm.202100383



clinical interventions, such as ultrasound imaging to assist and guide placement of the a-line, but with significant additional workload and, in the context of the coronavirus 2019 (COVID-19) pandemic, increased risk of exposure of frontline health-care workers to the virus.<sup>[12–15]</sup> A-lines are also highly restrictive

R. Avila, J. W. Kwak, Prof. Y. Huang, Prof. J. A. Rogers  
Department of Mechanical Engineering  
Northwestern University  
Evanston, IL 60208, USA

J. Vogl, Dr. A. Bradley, E. C. Dunne, C. M. Rand, Dr. D. E. Weese-Mayer  
Division of Pediatric Autonomic Medicine  
Department of Pediatrics  
Ann & Robert H. Lurie Children's Hospital of Chicago  
Chicago, IL 60611, USA  
E-mail: DWeese-Mayer@luriechildrens.org

A. Tzavelis  
Medical Scientist Training Program  
Feinberg School of Medicine  
Northwestern University  
Chicago, IL 60611, USA

Dr. H. U. Chung, J. Y. Lee, D. H. Kim, D. Ryu, S. S. Kim, J. Kim, J. B. Park,  
H. H. Jo  
Sibel Health  
Niles, IL 60714, USA

K. B. Fields, J. L. Ciatti, S. R. Madhupathy, Prof. Y. Huang,  
Prof. J. A. Rogers  
Department of Materials Science and Engineering  
Northwestern University  
Evanston, IL 60208, USA

S. Li, Prof. Y. Huang  
Department of Civil and Environmental Engineering  
Northwestern University  
Evanston, IL 60208, USA

M. Irie, Prof. J. A. Rogers  
Department of Electrical and Computer Engineering  
Northwestern University  
Evanston, IL 60208, USA

A. Shukla, J. Chavez, Dr. L. E. Marsillio, Dr. S. J. Hong  
Division of Critical Care  
Department of Pediatrics  
Ann & Robert H. Lurie Children's Hospital of Chicago  
Chicago, IL 60611, USA

Dr. S. Xu  
Department of Dermatology  
Division of Dermatology, and Department of Pediatrics  
Feinberg School of Medicine  
Northwestern University  
Chicago, IL 60611, USA

C. M. Rand, Dr. D. E. Weese-Mayer  
Stanley Manne Children's Research Institute  
Ann & Robert H. Lurie Children's Hospital of Chicago  
Chicago, IL 60611, USA

Dr. L. E. Marsillio, Dr. S. J. Hong, Dr. D. E. Weese-Mayer  
Department of Pediatrics  
Feinberg School of Medicine  
Northwestern University  
Chicago, IL 60611, USA

Dr. S. J. Hong  
Division of Neurology  
Department of Pediatrics  
Ann & Robert H. Lurie Children's Hospital of Chicago  
Chicago, IL 60611, USA

Prof. J. A. Rogers  
Department of Neurological Surgery  
Feinberg School of Medicine  
Northwestern University

in nature, with many hospitals electing to use cumbersome—albeit protective—accessories (e.g., padded splints, braces, tapes) to immobilize the puncture site and prevent any disturbance to the a-line itself, inevitably restricting natural movements of the patient.<sup>[16,17]</sup> While discrete, oscillometric cuff-based BP measurements avoid the ischemic, infectious, and procedural risks associated with a-lines, they do not offer continuous, beat-to-beat information, they can be inaccurate in BP extremes or in certain patients, and they can contribute to skin-related injuries (e.g., skin breakdown, pressure ulcers) for infant PICU patients.<sup>[18–20]</sup> With full consideration of these limitations, a clinical tool that could provide continuous, accurate, and beat-to-beat BP measurements, in a manner that is conducive to free body movement and is safe for sensitive pediatric skin, with minimal practitioner management and/or intervention, would be invaluable.

As described recently by our group, a simple pair of time-synchronized wireless, skin-interfaced devices, built according to the principles of soft hybrid electronics, can noninvasively capture continuous waveform and vital sign data (e.g., electrocardiography (ECG), photoplethysmography (PPG), heart rate (HR)) for neonatal and pediatric patients in ICUs.<sup>[21]</sup> Initial exploratory results suggest the use of pulse arrival time (PAT), defined as the time for a pulse to travel from the heart to a peripheral site (foot or hand), as a proxy for systolic BP (SBP). While SBP measurements are important in hemodynamic monitoring, they are inadequate for critically ill patients, for whom diastolic BP (DBP) provides valuable information about the risk for coronary artery malperfusion. SBP does not reliably predict DBP in critical illness and, therefore, requires its own independent measurements. A combination of PAT and HR is of interest for its strong correlation with both SBP and DBP in adult patients, and there currently exist Food and Drug Administration (FDA)-approved, wired clinical BP monitors, based on PAT and HR.<sup>[22–25]</sup> This multivariate analysis approach, for both SBP and DBP prediction, has not, however, been explored for patients in the PICU or neonatal ICU (NICU), nor has it been accomplished using wireless technologies relevant to these vulnerable subjects.

Our previously reported system features a binodal pair of devices, one that mounts on the chest and another that mounts on a limb, typically the hand or foot. This latter device performs PPG, in a most recent design that doubly wraps around the limb, with an umbilical interconnect that unites the two wrapping components.<sup>[21]</sup> Such a configuration demands extreme levels of bendability and, without optimized materials and layouts, it imposes constraints on the patient's range of motion, and it is susceptible to motion artifacts that can dramatically reduce the signal quality and reliability of the measurement.

This paper reports two sets of advances in this context. The first focuses on aspects of materials science and mechanical design that support a stable, yet soft and comfortable, interface between the limb unit and patients in the PICU, across a

Chicago, IL 60611, USA  
Prof. J. A. Rogers  
Department of Chemistry  
Northwestern University  
Evanston, IL 60208, USA

broad range of ages and body sizes. This component of the work includes quantitative, system-level studies by digital image correlation (DIC) methods, high-speed tracking techniques, and finite element analysis (FEA) simulations. The results, together with comparative analysis of various, low-modulus materials for device encapsulation and skin adhesion, yield devices optimized for pediatric uses, including procedures for sterilization that do not alter the operational characteristics or the properties of the constituent materials. Pilot studies based on 23 PICU patients and over 82 cumulative hours of recordings demonstrate reliable performance of these systems, without adverse events. The second part of the paper examines empirical relationships that connect key hemodynamic parameters associated with these recordings to both SBP and DBP. Comparisons to corresponding measurements performed with a-lines establish the accuracy of functional forms that include both HR and PAT, across a diverse patient cohort and set of pharmacological circumstances. The collective results suggest that wireless, soft electronics have the potential to significantly improve the care of patients in the PICU.

## 2. Results and Discussion

### 2.1. Wireless, Skin-Interfaced Devices in the PICU

Recently introduced wireless, skin-interfaced devices can provide ICU-grade monitoring of continuous waveform and vital sign data for neonatal and pediatric patients.<sup>[21]</sup> This noninvasive technology, comprised of flexible, stretchable electronic systems encapsulated with thin, soft, medical-grade polyorganosiloxane materials, features two separate devices that operate in a time-synchronized manner. The first device ("chest device"; weight:  $\approx 12$  g; dimensions:  $\approx 5$  cm  $\times$  3 cm  $\times$  0.6 cm (length  $\times$  width  $\times$  height)) mounts on the chest for measurements of 1) 1-lead ECG through gold-plated electrodes interfaced to the skin via a thin, conductive hydrogel adhesive (KM 40A, Katecho), 2) respiratory rate, seismocardiography, body orientation, activity levels, and vocal biomarkers (crying patterns) through a triaxial, high-bandwidth accelerometer, and 3) central-skin temperature via a clinical-grade temperature sensor. The second device ("limb device"; weight:  $\approx 9$  g; dimensions:  $\approx 9$  cm  $\times$  3 cm  $\times$  0.6 cm (length  $\times$  width  $\times$  height)) mounts on a peripheral extremity (foot or hand), secured with a soft wrap, for measurements of 1) transmission mode, dual-wavelength (red and infrared) PPG, from which blood oxygenation ( $\text{SpO}_2$ ) can be derived, and 2) peripheral-skin temperature via a clinical-grade temperature sensor. Images and schematic representations of the pair of devices (Figure 1A), as worn by a 37-week-old PICU patient (Figure 1B,C), highlight the contrast between this system and the wired collection of sensors that represent the current standard of care (Figure 1D,E).

Continuous and wireless device operation of up to 60 h relies on embedded, wirelessly rechargeable lithium-polymer batteries (60 mAh capacity) and Bluetooth low energy communication protocols. Data can be stored onto memory modules (4 GB storage capacity) within the devices themselves and/or live-streamed to a nearby connected Bluetooth-enabled device (e.g., iPad Pro), allowing for uninterrupted recording and acquisition of physiological waveforms and vital signs (Figure 1F).

### 2.2. Optimized System-Level Mechanics and Materials for the Peripheral Limb Device

The system-level layout, mechanics, and materials of the chest device remain relatively unchanged compared to those reported previously.<sup>[21]</sup> The focus here is on several advances in encapsulation design and material choices (unoptimized design (UD) versus optimized design (OD)) for the peripheral limb device (Figure 2A,B; Figure S1, Supporting Information), to improve their interfaces to peripheral limbs of pediatric patients (Figure 1C; Figure S2, Supporting Information). Here, an inner filler layer of OO-30 polyorganosiloxane elastomer (Ecoflex OO-30, Smooth-On) and an outer shell of A-20 polyorganosiloxane elastomer (Silbione RTV 4420, Elkem) encapsulate the device. This design proves to be a critical component for high signal quality data collection from transmission-mode PPG, as the dual-wavelength light-emitting diodes (LEDs) must maintain alignment with the photodetector upon wrapping around the small limbs of these patients. In particular, this configuration reduces the strain magnitude (Figure 2C,D; Video S1, Supporting Information) and shear strain (Figure 2E,F; Video S2, Supporting Information) distributions upon uniaxial stretching deformations of the serpentine wiring that connects the LEDs to the photodetector on the main body of the device. Experimental confirmation of the effects relies on DIC approaches that quantify the axial displacement of speckled surface patterns (Figures S3 and S4, Supporting Information), for accurate measurement of surface deformations.<sup>[26]</sup> Results show that the strain magnitude and shear strain profiles for the regions in between the LED unit and the photodetector ( $x = 18$  mm) at the edge regions of the OD decrease by  $\approx 33\%$  and  $\approx 96\%$ , respectively, compared to those of the UD devices (Figure 2G,H). Validated FEA simulations (Figures S5–S8, Supporting Information) complement these experimental results, illustrating the high strain concentration in the UD, compared to the minimal strains in the OD, as the device undergoes bending deformations (Figure 2I,J) that occur as the device wraps the hand or foot of a PICU patient. Figure 2K further highlights the differences in structural mechanics between the UD and OD, and importantly, the influence of the choice of soft materials for encapsulation. The OD, with an outer encapsulation shell of A-20 polyorganosiloxane elastomer and inner filler layer of OO-30 polyorganosiloxane elastomer, decreases the effective modulus by  $\approx 83\%$  and  $\approx 96\%$ , compared to that of the UD with the same materials and of the UD with the A-20 polyorganosiloxane as both the shell and filler, respectively (Figure S9, Supporting Information).

Another method to characterize the stiffness of the system is to compute the natural frequency and damping ratios of key structural components. The oscillatory behaviors for the LED units of the UD and OD can be captured by the high-speed tracking method.<sup>[27]</sup> As expected, both devices exhibit damped harmonic oscillations (Figure 2L; Video S3, Supporting Information), from which the natural (resonant) frequency and damping ratios are characterized (Figure 2M,N). The OD shows  $\approx 49\%$  and  $\approx 38\%$  decreases in natural frequency and damping ratio, respectively, compared to those of the UD. Fundamentally, experimental characterizations via DIC and the high-speed tracking method, complemented by FEA analyses, confirm that the OD, with its two-part polyorganosiloxane elastomer encapsulation and



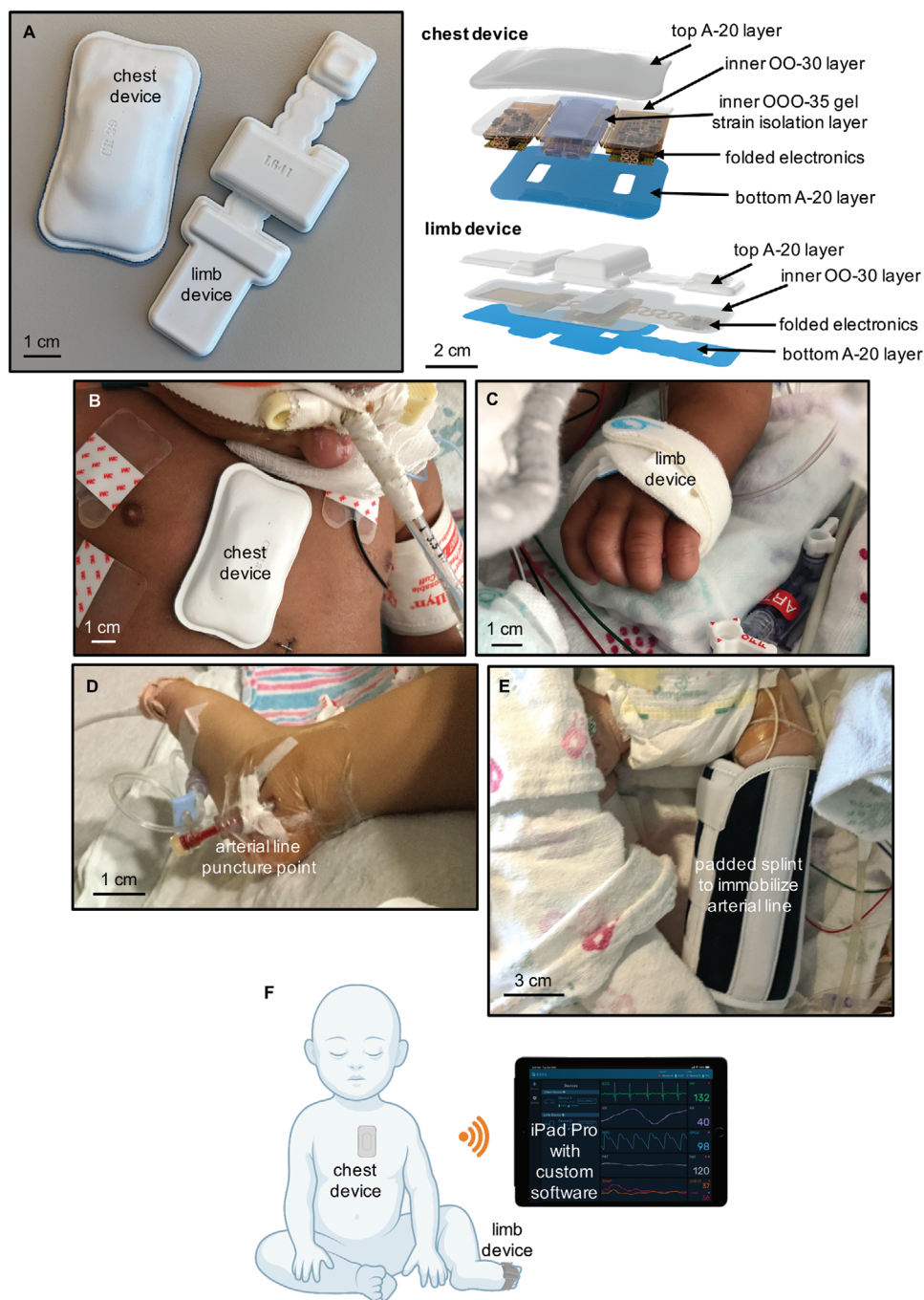


**Figure 1.** Soft, skin-interfaced devices for wireless measurements of blood pressure in pediatric intensive care unit (PICU) patients. A) Photograph (left) depicting a top-down view of the devices, and schematic representation (right) of the configurations and materials of the devices. The system consists of a chest device (capable of electrocardiography (ECG) measurements) and a limb device (capable of photoplethysmography (PPG) measurements). B) Photograph of a 37-week-old female patient in the PICU, wearing a chest device, flanked by conventional ECG adhesive electrodes and a blood pressure cuff. C) Photograph of the same patient in (B), wearing a limb device, secured with a soft velcro wrap, around the left hand. D) Photograph of the indwelling arterial line puncture point at the right dorsalis pedis artery of a 50-week-old male patient in the PICU. The invasive arterial line, which is oversized relative to the infant's foot, poses risk for ischemia and infection. E) Photograph of a 5-week-old male patient in the PICU, wearing a restrictive padded splint to immobilize and protect the indwelling arterial line puncture point at the left posterior tibial artery. In contrast to the devices shown in (A), (B), and (C), the arterial line and its associated accessories heavily limit free, natural body movement. F) Schematic representation of an infant with the wireless, skin-interfaced devices, which transmits physiological waveform and vital sign data to a nearby iPad Pro.

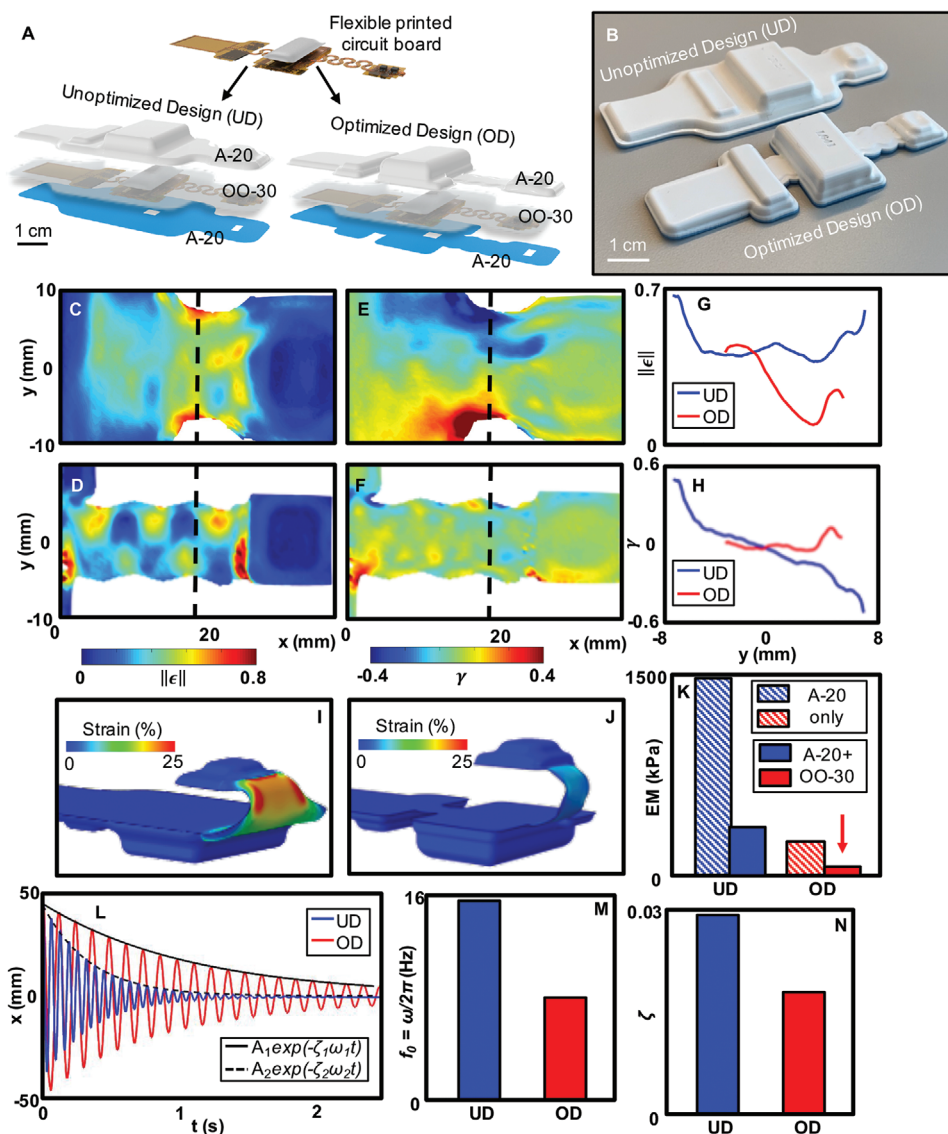


**Figure 2.** Optimized mechanics for robust wrapping of a soft, skin-interfaced wireless monitoring device around peripheral limbs. A) 3D rendering of the unencapsulated, flexible printed circuit board for the limb device and the encapsulation schemes, featuring the unoptimized design (UD) and optimized design (OD). Polyorganosiloxane elastomers, denoted by the manufacturer's listed Shore hardness, are used for the outer encapsulation shell (A-20, white/blue) and inner filler layer (OO-30, transparent). B) Photograph of the fully encapsulated limb devices. Experimental results via Digital Image Correlation of C,D) strain magnitude and E,F) shear strain for UD and OD, respectively, at 10% stretch. G) Strain magnitude and H) shear strain profiles at  $x = 18$  mm. FEA simulations of strain distribution in the encapsulation layer for bending deformations of I) UD and J) OD. K) Effective moduli (EM) of the device, computed via FEA, for UD (blue) and OD (red). Striped shading indicates that A-20 is used for both the outer encapsulation shell and inner filler layer, whereas solid shading indicates that A-20 is used for the outer encapsulation shell and OO-30 is used for the inner filler layer. L) Experimental results of oscillation via the tracking method; initial release at  $90^\circ$ . M) Natural frequencies and N) damping ratios of UD and OD.

space-efficient encapsulation design, enhance the soft mechanical properties of the system, of critical importance for wrapping small peripheral limbs of pediatric patients. To adhere and secure the limb device with the OD in place, the soft fabric wrap utilizes a velcro hook and loop dot to complete full wrapping of the device around the peripheral limb. Hydrogel pieces can also be integrated with the bottom surface of the device (Figure S20, Supporting Information) to enable adhesion to the skin.

### 2.3. Characterization of Soft Materials Used for Device Encapsulation and Skin Adhesion

As FEA simulations indicate (Figure 2K; Figure S9, Supporting Information), soft materials are important factors in determining the effective mechanical properties of the overall system. Thus, the compatibility of these devices with the sensitive, fragile skin of PICU patients relate directly to the use of such materials (e.g., polyorganosiloxane elastomers and gels), for both device



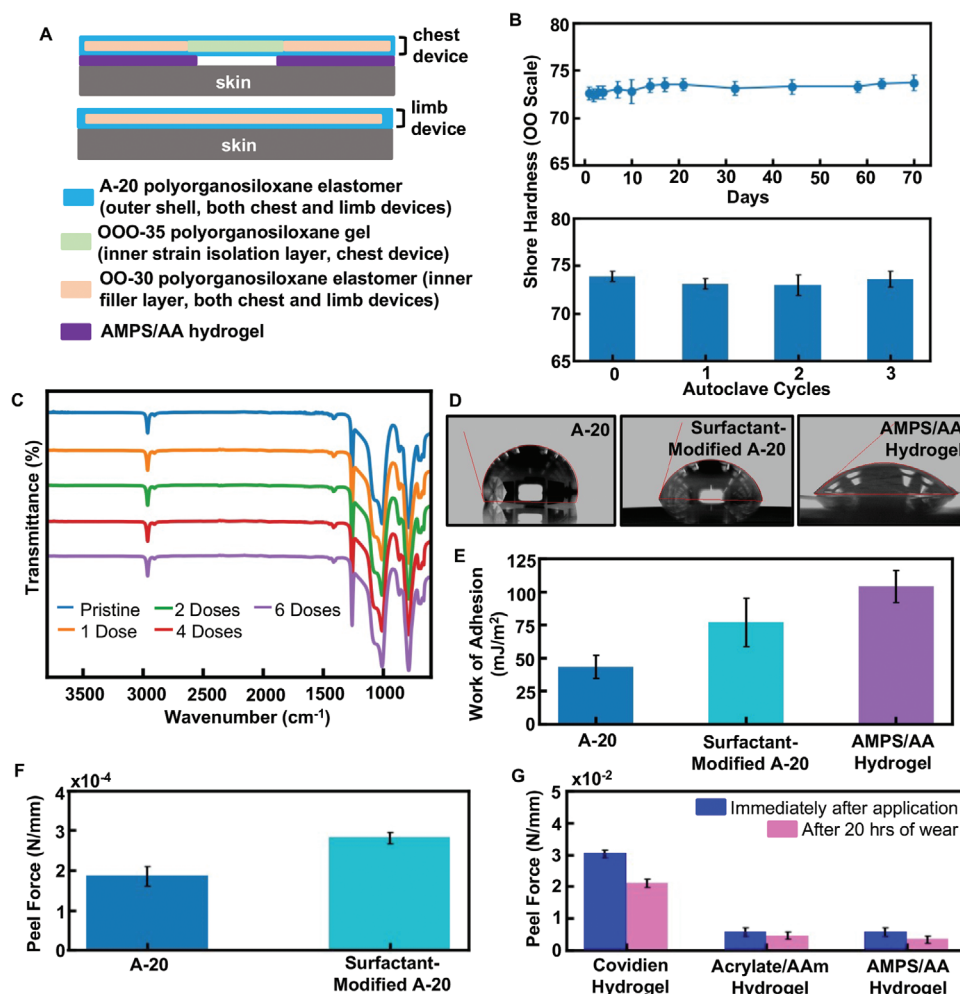


**Figure 3.** Characterization of soft materials used for wireless, skin-interfaced device encapsulation and their adhesion to the skin. A) Schematic representation of the cross-sectional, layer-by-layer soft materials stack for the chest device (top) and the limb device (bottom). Polyorganosiloxane elastomer and gel materials are denoted by the manufacturer's listed Shore hardness. B) Mechanical stability of dyed A-20 polyorganosiloxane elastomer, as a function of the number of days of shelf aging (top) and the number of autoclave exposure cycles (bottom). C) FTIR transmission spectra of A-20 polyorganosiloxane elastomer ( $\approx 30 \mu\text{m}$  thickness), as a function of the number of UVC exposure doses. D) Representative water contact angle images of A-20 polyorganosiloxane elastomer (left), surfactant-modified A-20 polyorganosiloxane elastomer (center), and AMPS/AA hydrogel (right). To improve hydrophilicity of the A-20 elastomer and compatibility with the AMPS/AA hydrogel, the surfactant (trisiloxane ethoxylate) modification can be employed. E) Work of adhesion, as derived from the Young–Dupre equation and water contact angle measurements. F) Peel force from  $90^\circ$  peel testing of AMPS/AA hydrogel on A-20 and surfactant-modified A-20 polyorganosiloxane elastomer substrates. G) Peel force from  $90^\circ$  peel testing on an adult with sensitive skin, for three hydrogel adhesives. Samples are immediately tested after application to the skin (blue) and after 20 h of wear (pink).

encapsulation/packaging and direct skin contact. The layered soft materials stack on the skin, for both the chest and limb device, is shown in **Figure 3A**. In the case of the chest device, a soft hydrogel (KM 40A, Katecho), based on the 2-acrylamido-2-methylpropane sulfonic acid/acrylic acid (AMPS/AA) copolymer, forms the conductive interface between the bottom layer (A-20 polyorganosiloxane elastomer)/gold-plated ECG electrodes of the device and the skin.

### 2.3.1. Stability of the A-20 Polyorganosiloxane Elastomer

Continuous and safe use of these devices in the ICU environment fundamentally requires the long-term stability and robustness

of the outer encapsulation shell material (A-20 polyorganosiloxane elastomer). Although many studies focus on the mechanical stability of polydimethylsiloxane (PDMS),<sup>[28–30]</sup> as a function of long shelf aging time periods at ambient conditions, limited data are available for other polyorganosiloxane elastomeric materials. Some studies suggest that certain commercial variants undergo softening and loss of compression strength over time, perhaps due to fillers, such as iron oxide, that induce cleavage of the siloxane backbone.<sup>[31,32]</sup> Additionally, residual fragments from organo-tin catalysts (e.g., tin dicarboxylates, dialkyltin dicarboxylates) typically used for condensation curing of these materials, together with ambient humidity, can significantly affect load-bearing properties, due to bond cleavage of the siloxane backbone and associated reduction of load-bearing polymer chains.<sup>[33,34]</sup>

Here, analysis of Shore hardness yields information on the mechanical stability of dyed A-20 polyorganosiloxane elastomer over a time period spanning more than two months (Figure 3B, top). Additional such measurements upon repeated exposure to high temperature (121 °C), humidity, and pressure conditions in an autoclave steam sterilizer, further confirm the mechanical stability of the material (Figure 3B, bottom). Both experiments in Figure 3B indicate that no significant changes occur under these conditions. The observations are particularly relevant for emerging uses of these devices in tropical or humid climates, such as those typically encountered in South America, Africa, and Asia. Battery-free devices<sup>[21,35]</sup> and designs that use removable batteries<sup>[21]</sup> can be sterilized within the autoclave, according to standard protocols.

In the ICU environment, UV germicidal irradiation is another common sterilization approach.<sup>[36]</sup> Here, light in the UVC region of the spectrum (200–280 nm) deactivates microorganisms and viruses that reside on common surfaces.<sup>[37,38]</sup> This method is increasingly popular in the context of the COVID-19 pandemic, as an energy-efficient, chemical-free method that can be effective at low exposure doses (3.7 and 16.9 mJ cm<sup>-2</sup> result in a 3-log reduction and full deactivation of SARS-CoV-2, respectively).<sup>[39]</sup> Studies of the stability of the A-20 polyorganosiloxane elastomer upon exposure to UVC are relevant in this context. Figure 3C shows Fourier transform infrared (FTIR) transmission spectra of A-20 polyorganosiloxane elastomer, at a thickness of ≈30 μm, as a function of cycles of exposure to UVC at a dose (31.8 mJ cm<sup>-2</sup>; narrow-band UVC, λ = 254 nm) that exceeds reported thresholds for significant log reduction and full deactivation of SARS-CoV-2 and other similar SARS-family viruses.<sup>[37–39]</sup> All spectra display the same stretching bands (e.g., the strong, broad peak (ν = 1008 cm<sup>-1</sup>) representative of the siloxane backbone (Si–O–Si) stretching, the strong, sharp peak (ν = 786 cm<sup>-1</sup>) representative of Si–C stretching), indicating no observable chemical change. Despite the small wavelengths of UVC, some studies have shown that UVC penetrates into the stratum corneum (≈30 μm thickness)—the outermost layer of the skin—inducing chemical damage.<sup>[40]</sup> Similarly, other studies have shown that UVC can overcome the thermodynamic energy barrier required to decompose both the Si–C (≈301 kJ mol<sup>-1</sup>) and Si–O–Si (≈447 kJ mol<sup>-1</sup>) bonds of certain polyorganosiloxane rubbers.<sup>[41]</sup> Photons in the UVC wavelength range (254 nm) exceeds the energies of these bonds, leading to chain scission of the main backbone and associated side chains, eventually forming new radicals. The penetration depth at which UVC induces such chemical changes in polyorganosiloxanes, such as PDMS, is still under debate,<sup>[42]</sup> with some studies suggesting depths ranging from ≈20–30 nm<sup>[43]</sup> to ≈8–14 μm.<sup>[44]</sup> While FTIR is valuable for discerning specific functional groups in the bulk, any possible chemical changes induced in the ultrathin, near-surface region of these materials should be further investigated with more surface-sensitive techniques, such as near edge X-ray absorption fine structure (NEXAFS).<sup>[45]</sup> Regardless, radical fragments produced by photoirradiation are known to recombine,<sup>[45,46]</sup> and furthermore, polyorganosiloxane materials feature constant diffusion of residual oligomers to the surface (“recovery”).<sup>[46]</sup> Therefore, sufficiently thick layers of A-20, as the outer encapsulation shell for the chest and limb devices, should maintain compatibility with UVC sterilization techniques.

### 2.3.2. Surface Energy Modulation of A-20 as a Route for Improving Adhesion to Hydrogels

Pristine polyorganosiloxanes are intrinsically hydrophobic, and they have low surface energies with poor wettability. By contrast, hydrogels consist of a hydrophilic macromolecular polymer network structure, and typically possess high surface energy. As the de Bruyne empirical rule of adhesion postulates, the incompatibility and weak matching of surface polarities between these two classes of materials leads to poor adhesive bonding properties between them.<sup>[47,48]</sup> Thus, the integration of such dual opposing surface energy materials into a singular device system, such as in the case of the interfacial contact between the A-20 bottom layer of the chest device and the conductive AMPS/AA hydrogel, may benefit from increases in the surface energy of the A-20 polyorganosiloxane elastomer. Here, changes in the water contact angle (WCA) between pristine A-20 (111° ± 3°) and A-20 modified with a trisiloxane ethoxylate (Silwet L-77, Bioworld) surfactant (83° ± 4°) indicate an increase in the hydrophilicity and surface energy of the surfactant-modified A-20 (Figure 3D), approaching values close to that of the AMPS/AA hydrogel (49° ± 3°).

The surface energy properties appear in the Young–Dupre equation,<sup>[49]</sup> which states that the thermodynamic work (work of adhesion) required to separate two different interfacial phases (e.g., liquid and solid) to an infinite distance is related to the contact angle

$$W = \gamma (1 + \cos(\theta)) \quad (1)$$

where  $W$  is the work of adhesion (mJ m<sup>-2</sup>),  $\gamma$  is the surface tension of the liquid ( $\gamma_{\text{water/air}, 25^\circ\text{C}} = 71.99 \text{ mJ m}^{-2}$ ), and  $\theta$  is the contact angle. Figure 3E illustrates the work of adhesion between polar liquid water droplets and pristine A-20 (44 ± 9 mJ m<sup>-2</sup>), surfactant-modified A-20 (77 ± 18 mJ m<sup>-2</sup>), and the AMPS/AA hydrogel (104 ± 12 mJ m<sup>-2</sup>). As expected, the surfactant-modified A-20 increases (≈77%) the work of adhesion, confirming the effectiveness of this surfactant modification approach.

Figure 3F demonstrates results from 90° peel force testing of AMPS/AA hydrogel on pristine A-20 and surfactant-modified A-20 substrates. While the surfactant-modified A-20 exhibits a substantial increase (≈52%) in peel force compared to pristine A-20, consistent with increased adhesion with the hydrogel, the values are relatively small. Many factors, in addition to surface polarity/wettability, influence adhesion, including the specific nature of the chemical interactions (covalent, hydrogen, ionic, dispersion forces, etc.) between the materials, mechanical dissipation, and the topology of the adherend connections.<sup>[50,51]</sup> Additional investigations of these effects may lead to strategies for further improvements.

Figure 3G illustrates comparative results from similar peel testing of three commercial hydrogel adhesives on an adult with sensitive skin, including: 1) individually packaged neonatal tape strips (“Covidien Hydrogel”), 2) an acrylate/acrylamide (“Acrylate/AAM”) copolymer-based hydrogel (KM 30 E, Katecho), and 3) the AMPS/AA hydrogel. The measurements indicate that all three adhesives remain on the skin both immediately after application and after 20 h of wear, including during overnight sleep. The Acrylate/AAM and AMPS/AA hydrogel adhesives both require significantly less (≈81%) peel force compared to the



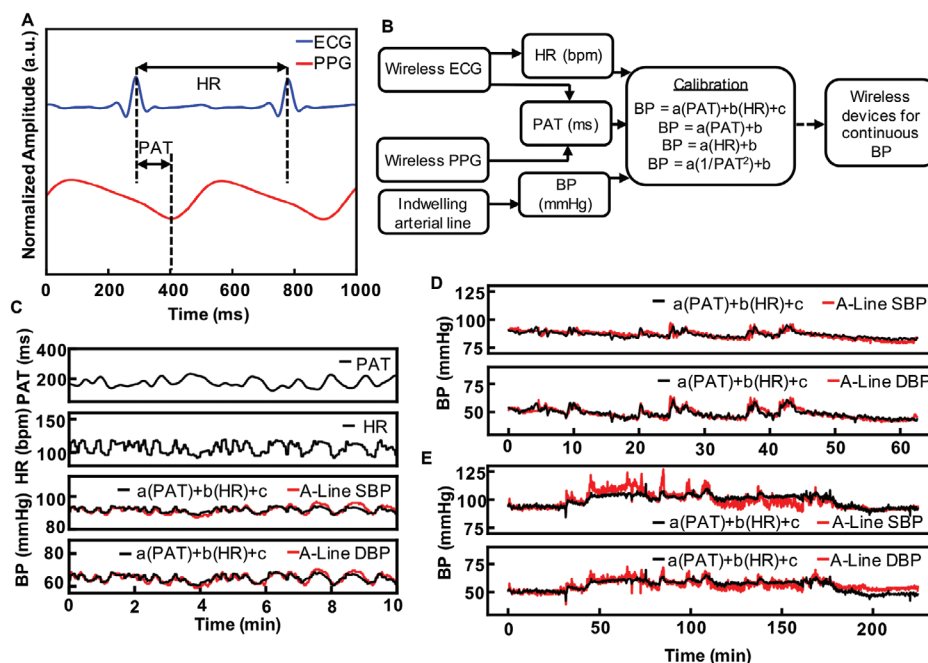


**Figure 4.** Pulse arrival time (PAT) and heart rate (HR) measured by wireless, skin-interfaced devices, as a proxy for continuous BP monitoring. A) Representative segments of time-synchronized and continuous electrocardiography (ECG) and photoplethysmography (PPG) recordings measured by the wireless, skin-interfaced chest and limb devices, respectively. From ECG and PPG, both PAT and HR can be derived. PAT is defined as the time delay between the ECG waveform R-peak and the onset of the PPG waveform at the peripheral limb device. HR is defined as the time interval between successive ECG waveform R-peaks. B) Flow diagram illustrating steps for time-synchronized data collection and calibration of pulse arrival time (PAT) and (HR) to blood pressure (BP). C) Representative example of an initial 10 min window of PAT and HR, which are then calibrated and converted into systolic BP (SBP) and diastolic BP (DBP) via the equation  $[a(PAT) + b(HR) + c]$ . Here, the obtained model equations are: SBP (mmHg) =  $[-0.02 \text{ ms}^{-1}(\text{PAT (ms)}) + 0.20 \text{ bpm}^{-1}(\text{HR (bpm)}) + 71.79 \text{ mmHg}]$ , and DBP (mmHg) =  $[-0.04 \text{ ms}^{-1}(\text{PAT (ms)}) + 0.24 \text{ bpm}^{-1}(\text{HR (bpm)}) + 38.42 \text{ mmHg}]$ . D) A 63 min recording of a 127-week-old female patient with acute hypoxemic respiratory failure, Trisomy 21, and multiple organ dysfunction. Comparisons between the  $[a(PAT) + b(HR) + c]$  model (black) and the arterial line (a-line) (red) are shown. E) A 225 min recording of a 47-week-old female patient with biliary atresia, status post liver transplant, and hypertension secondary to liver condition. Comparisons between the  $[a(PAT) + b(HR) + c]$  model (black) and the a-line (red) are shown.

Covidien hydrogel tape when immediately adhered to the skin. After 20 h of wear, however, the AMPS/AA hydrogel adhesive exhibits the smallest peel force ( $\approx 83\%$  and  $\approx 25\%$  less than Covidien hydrogel and Acrylate/AAM hydrogel, respectively). These characteristics are attractive for applications on fragile skin in the PICU setting, as the material optimally balances gentleness on the skin with long-term adherence for continuous ECG measurements.

## 2.4. Continuous BP Monitoring in the PICU with Wireless, Skin-Interfaced Devices, via PAT and HR

Time-synchronized ECG and PPG waveforms (Figure 4A) captured using these devices allow for calculations of the PAT, as defined by the time delay between the ECG waveform R-wave peak and the onset of the PPG waveform at the peripheral limb device. Also, HR, defined by the time interval between successive R-wave peaks can be derived.<sup>[21–25]</sup> Values of PAT and/or HR can be connected to BP through empirical relationships defined by model equations and calibration procedures (Figure 4B,C). The four model equations examined here range from a multivariate linear form<sup>[22–25]</sup>

$$\text{BP} = a(\text{PAT}) + b(\text{HR}) + c \quad (2)$$

to a univariate linear form<sup>[21–25,52,53]</sup>

$$\text{BP} = a(\text{PAT}) + b \quad (3)$$

$$\text{BP} = a(\text{HR}) + b \quad (4)$$

to a nonlinear inverse square relation<sup>[54]</sup>

$$\text{BP} = a\left(\frac{1}{\text{PAT}^2}\right) + b \quad (5)$$

in which BP can represent SBP or DBP. Figure 4D,E illustrates representative examples of continuous SBP and DBP recordings for: 1) a 127-week-old female patient with acute hypoxemic respiratory failure, Trisomy 21, and multiple organ dysfunction, and 2) a 47-week-old female patient with biliary atresia, status post liver transplant, and hypertension secondary to liver condition, respectively. In both cases, multivariate linear regression (Equation (2)) of the initial 10 min of PAT and HR data to the corresponding a-line BP data yield model coefficients (e.g.,  $a$ ,  $b$ ,  $c$ ) from which to estimate BP at subsequent times. These results highlight the agreement of BP determined in this manner with direct measurements using indwelling a-lines. This correspondence persists even through periods of significant fluctuations in BP.

**Table 1.** Baseline demographics and clinical characteristics ( $n = 23$  subjects).

Sex ( $n$ )	
Male	13
Female	10
Race/ethnicity ( $n$ )	
Caucasian	12
Hispanic/Latino	6
Black/African American	3
Asian	1
Other	1
At time of study (mean $\pm$ standard deviation)	
Age (weeks)	53 $\pm$ 47
Height (cm)	68 $\pm$ 15
Weight (kg)	8.2 $\pm$ 4.1
Arterial line location ( $n$ )	
Radial	17
Posterior tibial	4
Ulnar	1
Dorsalis pedis	1
Diagnoses ( $n$ )	
Acute respiratory failure	16
Respiratory syncytial virus	6
Seizures	3
Bronchopulmonary dysplasia from prematurity	2
Septic shock	2
Acute kidney injury	2
Metabolic crisis	1
Liver transplantation	4
Airway abnormality	2
Chronic respiratory failure	1

## 2.5. Evaluation of Model Performance for Prediction of BP

The studies include data collected from 23 PICU patients (Table 1), corresponding to a total of 290108 paired comparisons of SBP (Figure 5) and DBP (Figure 6) determined using data collected with the devices described in Figure 1 and measurements performed with indwelling a-lines. Bland–Altman plots (Figures 5A–D and 6A–D) describe the quantitative agreement between values determined using each of the four prediction models and the corresponding a-line results. For SBP prediction (Figure 5A–D), the mean and SD of the difference in BP is  $1.7 \pm 8.7$ ,  $0.3 \pm 12.2$ ,  $-1.9 \pm 11.4$ , and  $-1.1 \pm 76.1$  mmHg, corresponding to prediction models in Equations (2)–(5), respectively. The correlation matrix in Figure 5E summarizes the Pearson's product-moment correlation coefficient (“ $r$ ”) between each of the different models and the a-line SBP. The results indicate that the model with

the strongest linear relationship ( $r = 0.85$ ) with the a-line is, as expected, the multivariate PAT/HR model (Figure 5F). For DBP prediction (Figure 6A–D), the mean and SD of the difference in BP is  $1.8 \pm 6.2$ ,  $0.7 \pm 9.0$ ,  $-1.1 \pm 9.0$ , and  $0.5 \pm 9.7$  mmHg, respectively. The correlation matrix in Figure 6E also suggests that the multivariate PAT/HR model for DBP has the greatest linear correlation (Figure 6F) with the a-line ( $r = 0.77$ ).

The FDA recognizes consensus standards for evaluation of noninvasive BP measurements (ANSI/AAMI/ISO 81060–2:2013) that require that the mean and SD of the BP difference between the test device and the reference (e.g., indwelling a-line or cuff/stethoscope BP auscultation) is less than or equal to 5 and 8 mmHg, respectively, for adults.<sup>[55]</sup> The Bland–Altman results in our study (Figures 5A–D and 6A–D) indicate that the devices and analysis approaches (Equations (2)–(5)) meet these adult FDA specifications for measurements of DBP. For SBP, the mean difference, across all four models, is well within the 5 mmHg limit, the SD—of which the smallest value is 8.7 mmHg with the multivariate PAT/HR model—slightly eclipses the 8 mmHg criterion. Despite this marginal discrepancy, the results suggest that optimized wireless, skin-interfaced devices, when calibrated with the multivariate PAT/HR model, can yield acceptable quantitative equivalence to the clinical gold standard a-line for BP measurements in the PICU, as further evidenced by the strong statistical correlation between the comparative measurements (Figures 5E–F and 6E–F). An important fact is that, although the indwelling a-line is considered to be the clinical gold standard for BP measurements, the results can be subject to both over- and underestimation, due to improper dampening of waveforms.<sup>[56]</sup>

The aforementioned FDA consensus standard typically requires a sample size of at least 85 patients, determined from a power t-test with a 5% probability that a working device was rejected ( $\alpha = 0.05$ ) and a 2% probability ( $\beta = 0.02$ ) that an inaccurate device would be approved.<sup>[55,57]</sup> This criterion is specifically set for studies that utilize manual cuff/stethoscope auscultation as the BP reference. Due to challenges associated with recruitment of patients with indwelling a-line reference measurements, the FDA recommends that validation studies using invasive BP references to have a minimum sample size of 15 patients.<sup>[55,57]</sup> Therefore, the sample size ( $n = 23$  patients) used for the analyses presented here not only exceeds the required minimum, but the large amount of within-subject data (e.g., 290108 total observations from 23 patients = an average of 12613 observations per patient) provides sufficient statistical power for high confidence conclusions. Previous work suggests >99% power to detect significant associations with only 2400 nested observations, which this study exceeds.<sup>[58]</sup>

## 2.6. Changes in BP during and after Pharmacologic Interventions

Pharmacologic interventions are common in the PICU. Certain drugs can induce hemodynamic changes, as observed in measures of BP, HR, and PAT.<sup>[59–61]</sup> Figure 7 displays various examples of the ability of measurements using the wireless, skin-interfaced devices, with the multivariate PAT/HR model (Equation (1)), to capture such changes. Figure 7A shows the effects of enteral lorazepam, administered to a 75-week-old



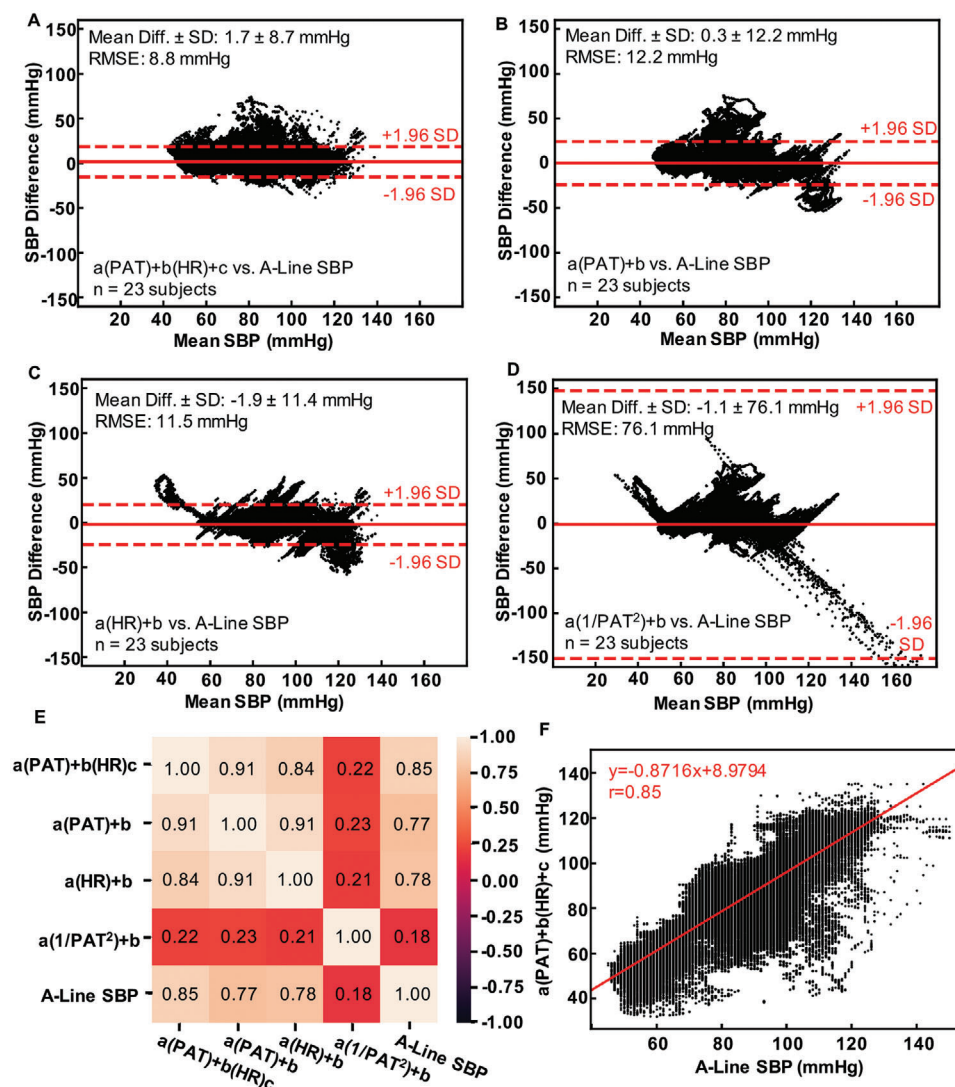


**Figure 5.** Comparisons of estimated systolic blood pressure (SBP) to arterial line (a-line) SBP ( $n = 23$  subjects; 290108 data points). A) Bland–Altman plots describing the difference in SBP values between the a-line and the  $a(PAT) + b(HR) + c$ , B)  $a(PAT) + b$ , C)  $a(HR) + b$ , and D)  $a(1/PAT^2) + b$  calibration models. Solid red lines indicate the mean differences in SBP measurements between the two modalities, whereas red dashed lines indicate 1.96 standard deviations (SD) above and below the mean differences (e.g., 95% limits of agreement). E) Correlation matrix describing the Pearson's product-moment correlation factor ( $r$ ) for SBP between the a-line and each calibration model. The  $a(PAT) + b(HR) + c$  calibration model displays the highest correlation coefficient ( $r = 0.85$ ) from comparison with the a-line SBP measurements. F) Scatterplot illustrating the linear correlation between the  $a(PAT) + b(HR) + c$  and a-line SBP measurements. The corresponding line of best fit ( $x = \text{A-Line SBP}$ ,  $y = a(PAT) + b(HR) + c$ ), with its equation and correlation coefficient, is shown in red.

patient with a history of bronchopulmonary dysplasia, due to extreme prematurity, and hospitalized for acute hypoxemic respiratory failure. Note the gradual increase in PAT (Figure 7A, first row), along with gradual decrease in HR (Figure 7A, second row) and both SBP and DBP (Figure 7A, third and fourth rows, respectively). The a-line SBP and DBP data also reflect these decreasing trends. All observed patterns are consistent with known sedative effects of lorazepam, a benzodiazepine.<sup>[62,63]</sup> Figure 7B shows the effects of methadone, a synthetic opioid analgesic, administered to an 8-week-old patient with seizures, severe anoxic brain injury, and multiple fractures. Note similar hemodynamic trends in PAT, HR, and BP, consistent with the known sedating narcotic effects of methadone.<sup>[64,65]</sup> Figure 7C

shows the effects of an intravenous dose of hydromorphone, a semisynthetic opioid analgesic, and morphine derivative, administered to a 101-week-old patient with Trisomy 21 and hospitalized for respiratory failure, due to respiratory syncytial virus bronchiolitis. Here, after administration, more frequent and dramatic oscillations appear in PAT, HR, SBP, and DBP, all of which the devices capture, and BP by the a-line. Such oscillatory hemodynamic patterns can occur after administration of opioid analgesics, notably morphine, and particularly in premature infants, but the physiological mechanism behind such oscillations is still unknown.<sup>[66–68]</sup> Figure 7D shows the response to an intravenous injection of dexamethasone, given to a 31-week-old patient hospitalized with seizures and acute hypoxemic

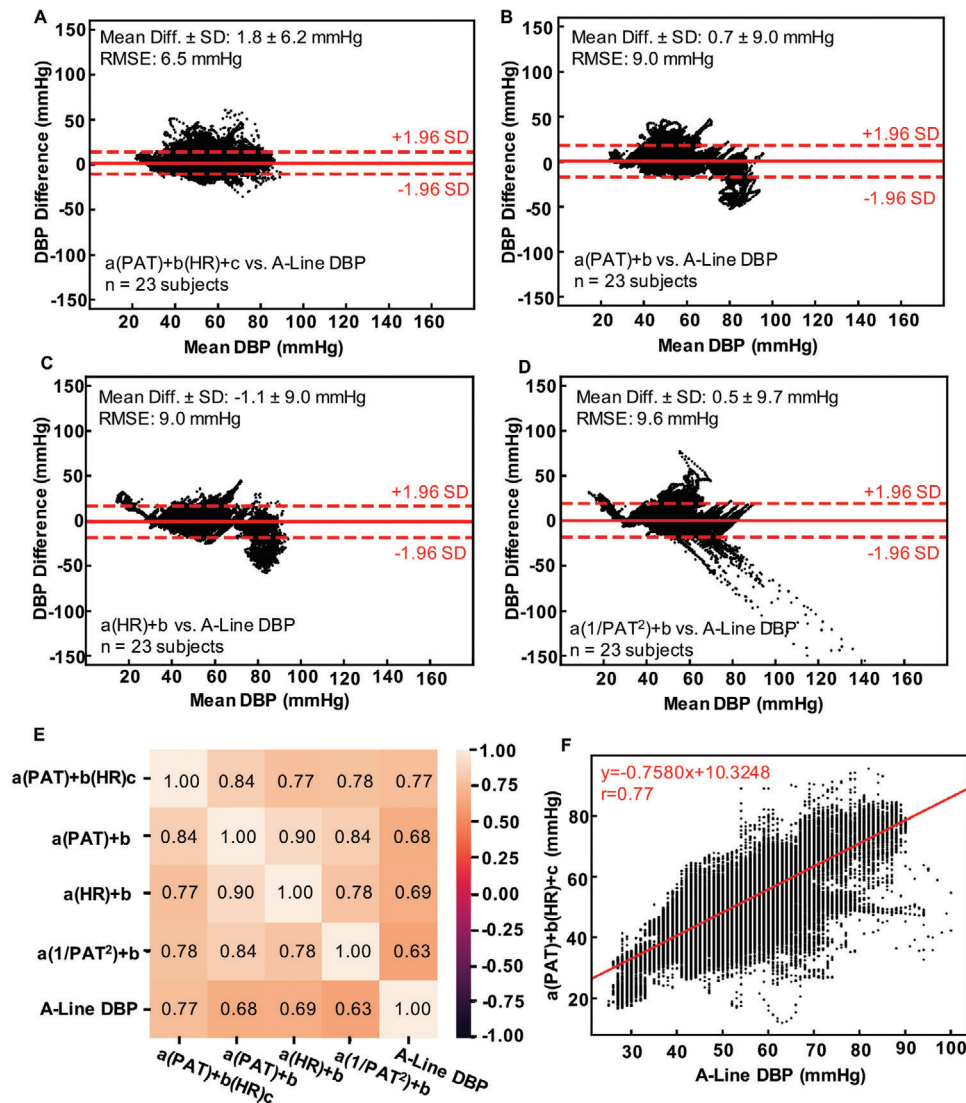


**Figure 6.** Comparisons of estimated diastolic blood pressure (DBP) to arterial line (a-line) DBP ( $n = 23$  subjects; 290108 data points). A) Bland–Altman plots describing the difference in DBP values between the a-line and the  $a(\text{PAT}) + b(\text{HR}) + c$ , B)  $a(\text{PAT}) + b$ , C)  $a(\text{HR}) + b$ , and D)  $a(1/\text{PAT}^2) + b$  calibration models. Solid red lines indicate the mean differences in DBP measurements between the two modalities, whereas red dashed lines indicate 1.96 standard deviations (SD) above and below the mean differences (e.g., 95% limits of agreement). E) Correlation matrix describing the Pearson's product-moment correlation factor ( $r$ ) for DBP between the a-line and each calibration model. The  $a(\text{PAT}) + b(\text{HR}) + c$  calibration model displays the highest correlation coefficient ( $r = 0.77$ ) from comparison with the a-line DBP measurements. F) Scatterplot illustrating the linear correlation between the  $a(\text{PAT}) + b(\text{HR}) + c$  and a-line DBP measurements. The corresponding line of best fit ( $x = \text{A-Line DBP}$ ,  $y = a(\text{PAT}) + b(\text{HR}) + c$ ), with its equation and correlation coefficient, is shown in red.

respiratory failure. Dexamethasone, a corticosteroid, is known to elevate HR and BP, with hypertension as a common side effect of the treatment.<sup>[69–71]</sup> Upon administration, a large rise in HR (Figure 7D, second row) appears, along with moderate increases in SBP and DBP (Figure 7D, third and fourth rows, respectively), all of which then return to a stable baseline. Measurements with the devices maintain reliable correlation with the a-line during these dramatic changes in HR. In all four cases, which feature distinct pharmacologic interventions and patients of differing ages and medical conditions, the devices, using the multivariate PAT/HR model, provide consistent performance with the a-line for BP measurements.

### 3. Conclusion

The collective outcomes from this study suggest that wireless, skin-interfaced devices can be optimized, through careful selection of materials and mechanics designs, for use in the PICU environment. The results support continuous, noninvasive measurements of vital signs and, through empirical models, SBP and DBP for patients with an accuracy comparable to the clinical gold standards, including those determined with indwelling a-lines. Importantly, these devices can capture immediate hemodynamic changes that occur after pharmacologic interventions, which may be useful in guiding further clinical management. The 23 PICU



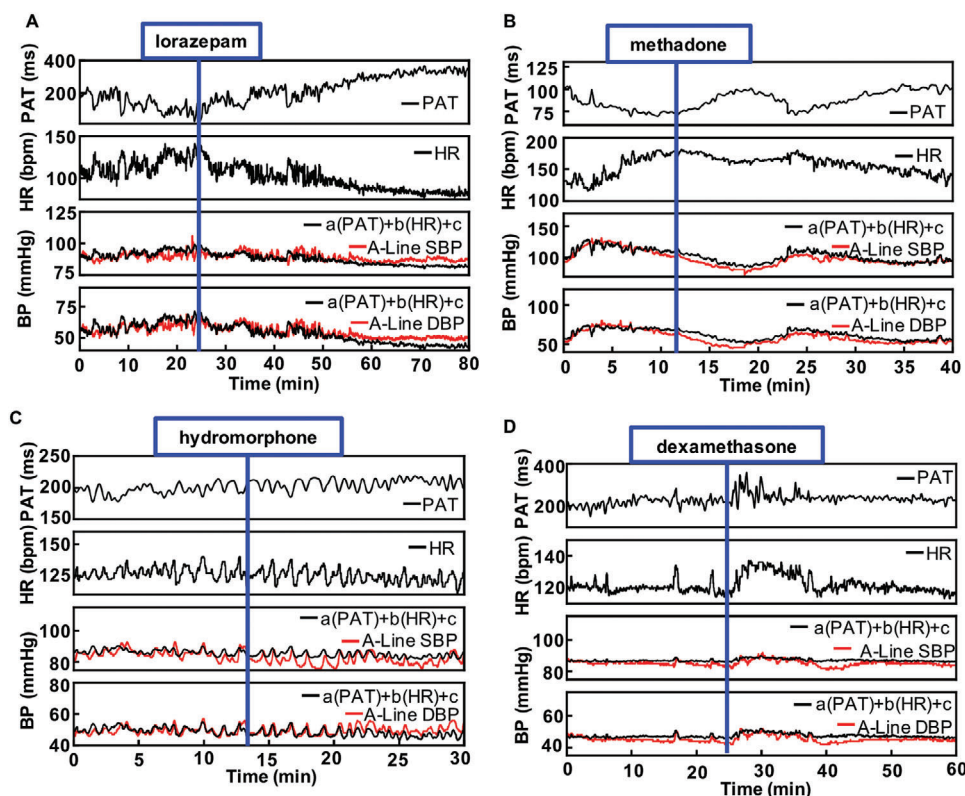


**Figure 7.** Performance of wireless, skin-interfaced devices, calibrated using  $[a(\text{PAT}) + b(\text{HR}) + c]$ , in capture of transient blood pressure and other hemodynamic changes after pharmacologic interventions. A) An 80 min recording of a 75-week-old male patient with bronchopulmonary dysplasia, history of extreme prematurity (gestational age of 23 weeks), and acute hypoxemic respiratory failure, featuring administration of enteral lorazepam at time = 24 min. B) A 40 min recording of an 8-week-old male with seizures, severe anoxic brain injury, and multiple fractures, featuring administration of methadone at time = 12 min. C) A 30 min recording of a 101-week-old male patient with respiratory syncytial virus bronchiolitis and Trisomy 21, featuring intravenous administration of hydromorphone at time = 13 minutes. D) A 60 min recording of a 31-week-old female patient with seizures and acute hypoxemic respiratory failure, featuring intravenous administration of dexamethasone at time = 23 min.

patients included in this study represent a pragmatic cohort of infants with a-line monitoring, most with respiratory failure for varying reasons, and a few with liver failure and airway abnormalities. The soft, flexible, and “pediatric-sized” design of the wireless, skin-interfaced devices described here are not only applicable, but also highly compatible with these PICU patients. These systems remove the restrictive burden of wired-based systems and mitigate the potential for skin-based issues or injuries that typically arise from use of these conventional physiologic monitoring systems. The noninvasive, wireless operation of these devices also minimizes the risks of ischemia, infection, and procedural difficulties typically associated with usage of a-lines.

The analyses presented here require an initial calibration period, when the indwelling a-line’s reference BP measurements are needed to convert the PAT and HR data into BP values. However, it would be more ideal to completely bypass the usage of the indwelling a-line for any initial calibrations or recalibrations due to its invasive nature. Thus, an alternative clinical case scenario would be to simply use a noninvasive BP reference for calibration, such as the oscillometric cuff, which has been similarly implemented by the FDA-approved, wired Sotera Visi system, thereby eliminating any need for the a-line.<sup>[24,25]</sup>

Naturally, the application of these wireless, skin-interfaced devices can be extended outside of the ICU environment for use in

both the outpatient ambulatory setting and the in-home setting, as means for continuous monitoring and tracking of patients discharged from the ICU. To enable real-time monitoring of BP for the user, the desired calibration algorithm, such as the multivariate PAT/HR model, can be implemented within the software of the tablet application. Any potential recurrences of health emergencies or vital sign abnormalities could then quickly be transmitted to clinicians to guide further therapeutic decision-making.

Long-term, continuous monitoring of the devices is enabled by robust adhesion of the devices to the skin. In the case of the chest device, a soft AMPS/AA-based hydrogel maintains the conductive, adhesive interface between the device and skin (Figure 3G). For the limb device, a soft fabric velcro wrap and optional use of the hydrogel (Figure S20, Supporting Information) adheres and maintains the alignment and positioning of the LED and photodetector components required for PPG measurements. Additional methods for securing the limb device in place are to utilize socks or mittens, depending on the location of device placement.

To our knowledge, this study is the first systematic inquiry that explores the correlation between continuous noninvasive and invasive BP measurements in the PICU. The results are highly promising, but they also underscore the need for further clinical investigations with larger cohort sizes and of

different ICU patient populations (e.g., neonatal critical care, neurocritical care, cardiac critical care, across a broader age range). Future directions, including examination of the potential causes for observed interpatient variability (Figures S16 and S17, Supporting Information), such as disrupted autonomic regulation of hemodynamics,<sup>[72]</sup> will yield further insights that may improve the overall monitoring accuracy.

## 4. Experimental Section

**Encapsulation of the Chest and Limb Devices:** General details on the assembly and encapsulation of the chest device can be found elsewhere.<sup>[21]</sup> To provide strain isolation of the center island of the flexible printed circuit board (fPCB) of the chest device, a low-modulus ( $\approx 4$  kPa) polyorganosiloxane gel ("OO-35"; Ecoflex Gel, Smooth-On) was used to completely enclose the island. Additionally, due to the sticky nature of the OO-35 gel, the center island of the fPCB was then adhered and secured onto the center position of the bottom encapsulation layer, consisting of a thin ( $\approx 500$   $\mu$ m) polyorganosiloxane elastomer ("A-20") film (1:1 w:w Silbione RTV 4420, Elkem, mixed with 5 wt% silicone opaque dye (Silc-Pig, Smooth-On)). The rest of the inner space of the chest device was filled with another polyorganosiloxane elastomer ("OO-30"; Ecoflex OO-30, Smooth-On). For the limb device, the assembly and encapsulation process started with folding the fPCB to reduce the overall size of the device. To completely enclose the folded device, top (white) and bottom (blue) encapsulation shell layers were designed for each device. These encapsulation layers were thin ( $\approx 500$   $\mu$ m) A-20 films (1:1 w:w Silbione RTV 4420, Elkem, mixed with 5 wt% silicone opaque dye (Silc-Pig, Smooth-On)) were formed by using a pair of concave and convex aluminum molds and thermal curing at 100 °C for 20 min. The folded device was placed in between these cured A-20 top and bottom encapsulation layers. To avoid tearing of the A-20 encapsulation layers from the fPCB or from mechanical deformations, such as bending or twisting, the empty space in between the A-20 encapsulation layers and the device was filled with OO-30. This material, with low modulus (0.069 MPa), provided improved softness. The molds with these materials were overlaid and bonded from thermal curing (100 °C for 20 min), finishing the encapsulation process.

**Digital Image Correlation (2D-DIC) Experiments:** The experiments involved recording uniaxial-stretched devices using a high-speed camera (2048  $\times$  1088 resolution, HT-2000M, Emergent) with 35 mm imaging lenses (F1.4 manual focus, Kowa) at the frame rate of 100 fps. The devices were uniformly coated with black speckles (Figure S3, Supporting Information), size of  $\approx 200$ –500  $\mu$ m, by the spray-painting method. The open-source 2D-DIC software, Ncorr, was used to measure material deformation of the devices.<sup>[26]</sup> To achieve high resolution and accurate deformation characteristics, DIC subset radius and spacing were set as 700  $\mu$ m and spacing of 140  $\mu$ m, resolving over 30 000 displacement grids. Strain magnitude and shear strain were computed based on the Triangular Cosserat Point Theory.<sup>[73]</sup>

**High-Speed Tracking Experiments:** The same set of hardware, as the DIC experiments, was used to record the oscillations of the devices. The sides of the LED units were painted black, and the image set was recorded at 500 Hz to accurately track their fast oscillations. Both devices were fixed vertically, and their LED units were initially bent 90° before the release. Both systems were recorded until the oscillations were completely damped to capture the full dynamics ( $>4000$  frames). The centers of the LED units were detected in a subpixel level, tracked using the Hungarian algorithm, and linked by performing a five-frame gap closing to produce a single, long, oscillating trajectory for each system. More details on the tracking method can be found elsewhere.<sup>[27]</sup>

**FEA Simulations:** The commercial FEA software, ABAQUS, was utilized to determine the mechanical performance of the metal serpentine interconnects and the encapsulation design of the devices. The objectives of the analysis were to ensure no plastic deformation (i.e.,  $\epsilon < 0.3\%$ ) occurs in 1) the copper (Cu) layer interconnects when the device undergoes different types of external loads (e.g., stretching, bending, twisting, and

wrapping around the foot), and 2) reduce the magnitude of the strain in the optimized soft encapsulation. The effective modulus of the design types was calculated from the slopes in Figure S9 of the Supporting Information and approximate cross-sectional area in the stretching region (UD  $\approx 45$  mm<sup>2</sup> and OD  $\approx 9$  mm<sup>2</sup>), based on the uniaxial stretching results in Figure S8 of the Supporting Information. The thin Cu ( $\approx 18$   $\mu$ m thick) layers were modeled by composite shell elements (S4R), and the soft encapsulation was modeled by hexahedron elements (C3D8R). The element size was tested to ensure the convergence and the accuracy of the simulation results. The elastic modulus ( $E$ ) and Poisson's ratio ( $\nu$ ) were  $E_{PI} = 2.5$  GPa and  $\nu_{PI} = 0.34$  for polyimide (PI);  $E_{Cu} = 119$  GPa and  $\nu_{Cu} = 0.34$  for copper;  $E_{A-20} = 0.8$  MPa and  $\nu_{A-20} = 0.5$  for A-20 polyorganosiloxane elastomer (Silbione RTV 4420, Elkem);  $E_{OO-30} = 60$  kPa and  $\nu_{OO-30} = 0.5$  for OO-30 polyorganosiloxane elastomer (Ecoflex OO-30, Smooth-On).

**Shelf Aging:** A-20 polyorganosiloxane elastomer (Silbione RTV 4420, Elkem) was prepared by mixing part A and B (1:1 w:w ratio) and 5 wt% silicone opaque dye (Silc-Pig, Smooth-On) in a two-step process in a planetary centrifugal mixer (Thinky ARE-310): 1) for 30 s at 2000 RPM, 2) 30 s at 2200 RPM, degassed for 3 min in a 90 mm petri dish, and cured in a 70 °C oven for 2 h. Shore hardness measurements were taken with a Type OO Shore durometer (Model 1600, Rex Gauge Company Inc.), mounted on an operating stand (Model OS-4H, Rex Gauge Company Inc.). Presented results are the average of measurements taken from five locations per sample, and propagated uncertainty (e.g., the square root of the sum of the 1) squared standard deviation of measurements taken from five locations per sample, and the 2) squared instrument precision (0.5 OO scale)).

**Autoclave Sterilization:** A-20 polyorganosiloxane elastomer (Silbione RTV 4420, Elkem) was prepared by mixing part A and B (1:1 w:w ratio) and 5 wt% silicone opaque dye (Silc-Pig, Smooth-On) in a two-step process in a planetary centrifugal mixer (Thinky ARE-310): 1) for 30 s at 2000 RPM, 2) 30 s at 2200 RPM, degassed for 3 min in an aluminum foil-lined 90 mm petri dish, and cured in a 70 °C oven for 2 h. Samples were placed in the autoclave steam sterilizer (Heidolph Tuttner 3545E Autoclave Sterilizer, Electronic Model AE-K), to undergo one exposure cycle, at a temperature of 121 °C, for a total of 75 min (15 min sterilization time, 60 min drying time). Shore hardness measurements, taken 24 h after each exposure cycle, were taken with a Type OO Shore durometer (Model 1600, Rex Gauge Company Inc.), mounted on an operating stand (Model OS-4H, Rex Gauge Company Inc.). Presented results are the average of measurements taken from five locations per sample, and propagated uncertainty (e.g., the square root of the sum of the 1) squared standard deviation of measurements taken from five locations per sample, and the 2) squared instrument precision (0.5 OO scale)).

**UVC Exposure:** A-20 polyorganosiloxane elastomer (Silbione RTV 4420, Elkem) was prepared by mixing part A and B (1:1 w:w ratio) in a two-step process in a planetary centrifugal mixer (Thinky ARE-310): 1) for 30 s at 2000 RPM, 2) 30 s at 2200 RPM, and degassed for 3 min afterward. Samples were formed by spin-coating the A-20 mixture on glass slides at 3000 RPM for 30 s and subsequent curing in a 70 °C oven for 15 min, yielding  $\approx 30$   $\mu$ m thick substrates. The samples were placed in a dark, enclosed chamber lined with aluminum foil, with a slit opening on top for direct exposure from a continuous, constant intensity, and narrow-band ( $\lambda = 254$  nm) 8 W UV lamp (UVLS-28, Analytik Jena). A digital UVC radiometer (Model 8.0 UVC, Solarmeter), placed at the same point of exposure as the samples, measured UVC intensity ( $\mu$ W cm<sup>-2</sup>), allowing for determination of exposure dosage values.

**FTIR Spectroscopy:** Solid state FTIR transmission spectra of the prepared A-20 polyorganosiloxane elastomer (Silbione 4420, Elkem) samples were collected with the use of a Thermo Scientific Nicolet iS50, over a range from 4000 to 400 cm<sup>-1</sup>. FTIR (cm<sup>-1</sup>):  $\nu = 2962$  (w;  $\nu_{as}$ (C–H)), 1257 (m;  $\nu_s$ (C–H)), 1008 (s;  $\nu$ (Si–O–Si)), 786 (s;  $\nu$ (Si–C)).

**Fabrication of Surfactant-Modified A-20 Polyorganosiloxane Elastomer:** Surfactant-modified A-20 polyorganosiloxane elastomer (Silbione RTV 4420, Elkem) was prepared by mixing part A and B (1:1 w:w ratio) and 0.2 wt% trisiloxane ethoxylate surfactant (Silwet L-77, Bioworld)<sup>[74]</sup> in a two-step process in a planetary centrifugal mixer (Thinky ARE-310): 1) for 30 s at 2000 RPM, 2) 30 s at 2200 RPM. Samples were formed by spin-coating the surfactant-modified A-20 mixture on glass slides at 250 RPM for 30 s

and subsequent curing in a 70 °C oven for 15 min, yielding ≈200 µm thick substrates.

**WCA Measurements:** Static WCA measurements were taken from 2 µL deionized water droplets using a video contact angle system (VCA Optima XE, AST Products). Presented results are the average and standard deviation of 5 WCA measurements taken per sample.

**Peel Force Measurements on A-20 and Surfactant-Modified A-20 Polyorganosiloxane Elastomer:** A-20 polyorganosiloxane elastomer (Silbione RTV 4420, Elkem) was prepared by mixing part A and B (1:1 w:w ratio) in a two-step process in a planetary centrifugal mixer (Thinky ARE-310): 1) for 30 s at 2000 RPM, 2) 30 s at 2200 RPM, and degassed for 3 min afterward. Samples were formed by spin-coating the A-20 mixture on glass slides at 250 RPM for 30 s and subsequent curing in a 70 °C oven for 15 min. Surfactant-modified A-20 polyorganosiloxane elastomer (Silbione RTV 4420, Elkem) was prepared by mixing part A and B (1:1 w:w ratio) and 0.2 wt% trisiloxane ethoxylate surfactant (Silwet L-77, Bioworld) in a two-step process in a planetary centrifugal mixer (Thinky ARE-310): 1) for 30 s at 2000 RPM, 2) 30 s at 2200 RPM. Samples were formed by spin-coating the surfactant-modified A-20 mixture on glass slides at 250 RPM for 30 s and subsequent curing in a 70 °C oven for 15 min.

AMPS/AA hydrogel (KM 40A, Katecho) strips of 20 mm width were adhered to these samples, and a unit magnetic weight (#5862K23, McMaster-Carr) was attached, one-by-one, to one end of the sample, such that the peel angle was 90°. The minimum weight required to peel and detach the adhesive was recorded. Presented results are the average and standard deviation of four trials.

**Peel Force Measurements on Skin:** Covidien hydrogel (Argyle Hydrogel Adhesive Baby Tape Strips, Covidien), Acrylate/AAm hydrogel (KM 30 E, Katecho), and AMPS/AA hydrogel (KM 40A, Katecho) strips of 20 mm width were adhered to the pre-cleaned, left ventral forearm of an adult female with sensitive skin, and a unit magnetic weight (#5862K23, McMaster-Carr) was attached, one-by-one, to one end of the adhesive sample, such that the peel angle was 90°. The minimum weight required to peel and detach the adhesive was recorded, both immediately after application to the skin, and after 20 h of wear (including during overnight sleep).

**Clinical Study Design:** The Institutional Review Boards of Ann & Robert H. Lurie Children's Hospital of Chicago (IRB 2018-1668) and Northwestern University (STU00208150) approved the protocol for this prospective, single-center, observational pilot study. Eligible patients included any patient under three years of age admitted to the PICU at the Ann & Robert H. Lurie Children's Hospital of Chicago, who possessed an indwelling a-line for continuous BP monitoring for clinical care. Informed consent for participation was obtained from all patients' legal guardians.

**Device Application and Data Collection:** After following a sterilization process approved by the infection control committee of the Ann & Robert H. Lurie Children's Hospital of Chicago,<sup>[21]</sup> the chest device was applied onto the chest, without interfering with existing standard of care equipment and secured with AMPS/AA hydrogel adhesive (KM 40A, Katecho). The limb device was wrapped around a peripheral extremity (foot or hand), free of existing standard of care equipment, and secured with a soft velcro wrap. Both devices wirelessly connect to an iPad Pro, enabling data transmission, collection, and storage. Indwelling a-line recordings of SBP and DBP were extracted from the Philips Intellivue MX800 patient monitor with the BedMaster software. Devices were removed to allow certain procedures (e.g., MRI imaging, ultrasounds, surgery, baths) take place. A list of clinically administered drugs and times of administration during the data collection period was recorded in the Epic electronic medical record system.

**Data Processing:** PAT and HR data were downloaded from the devices' internal memory and subsequently time-synchronized to systolic and diastolic BP data from the indwelling a-line. PAT, HR, SBP, and DBP data were removed during periods of data collection in which the devices were either disturbed or removed (e.g., medical procedures). Likewise, the indwelling a-line data were removed during periods when the BedMaster software malfunctioned or the lines were disturbed (e.g., the line was being replaced or flushed).

**Calibration Procedure:** For each patient, an initial 10 min window of PAT and/or HR data, measured by the wireless, skin-interfaced devices were calibrated to corresponding SBP and DBP data from the indwelling a-line, using the relationships given by Equations (2)–(5). Ordinary least squares regression, using the Python *statsmodel* module, defined the optimal model coefficients (e.g., *a*, *b*, *c*). These coefficients were then applied to the remaining PAT and/or HR data to estimate SBP and DBP. Recalibration was not performed for any patient.

**Post Hoc Statistical Analysis:** Comparisons of BP measurements between the wireless, skin-interfaced devices and the indwelling a-line were evaluated using the Python Pandas pairwise correlation matrix function. Bland–Altman analysis was used to determine the level of agreement between the two modalities, featuring 290108 paired data points obtained from 23 subjects. Paired t-tests, using the Python *statannot* package were used to determine statistical significance of the differences of the two modalities. Significance was applied to *p* < 0.05.

## Supporting Information

Supporting Information is available from the Wiley Online Library or from the author.

## Acknowledgements

C.L., J.-T.K., S.S.K., and A.H.-F. contributed equally to this work. D.E.W.-M., C.M.R., and J.A.R. acknowledge funding support from the Gerber Foundation. C.L. and S.R.M. acknowledge funding support from the National Science Foundation Graduate Research Fellowship Program (NSF DGE-1842165). This work made use of the Keck-II facility and the NUFAB facility of Northwestern University's NUANCE Center, which has received support from the SHyNE Resource (NSF ECCS-2025633), the IIN, and Northwestern's MRSEC program (NSF DMR-1720139). Engineering efforts were supported by the Querrey Simpson Institute for Bioelectronics at Northwestern University. The authors gratefully acknowledge the late Dr. Lauren E. Marsillio for her contributions to this work. The authors also thank all of the patients and their families who participated in this study, as well as the PICU staff of the Ann & Robert H. Lurie Children's Hospital of Chicago.

## Conflict of Interest

The authors declare no conflict of interest.

## Data Availability Statement

Research data are not shared.

## Keywords

blood pressure, hemodynamics, pediatrics, soft electronics, vital signs monitoring, wireless wearables

Received: February 28, 2021

Revised: March 22, 2021

Published online: May 3, 2021

[1] W. P. de Boode, *Early Hum. Dev.* **2010**, *86*, 137.

[2] H. B. Gershengorn, H. Wunsch, D. C. Scales, R. Zarychanski, G. Rubinfeld, A. Garland, *JAMA Intern. Med.* **2014**, *174*, 1746.



- [3] H. B. Gershengorn, A. Garland, A. Kramer, D. C. Scales, G. Rubenfeld, H. Wunsch, *Anesthesiology* **2014**, *120*, 650.
- [4] J. C. Lucet, L. Bouadma, J. R. Zahar, C. Schweber, A. Geffoy, S. Pease, M. C. Herault, H. Haouache, C. Adrie, M. Thuong, A. Francais, M. Garrouste-Orgeas, J. F. Timsit, *Crit. Care Med.* **2010**, *38*, 1030.
- [5] J. R. Gowardman, J. Lipman, C. M. Rickard, *J. Hosp. Infect.* **2010**, *75*, 12.
- [6] L. Zhang, J. Gowardman, M. Morrison, L. Krause, C. M. Rickard, *Eur. J. Clin. Microbiol.* **2014**, *33*, 1189.
- [7] A. Rhodes, L. E. Evans, W. Alhazzani, M. M. Levy, M. Antonelli, R. Ferrer, A. Kumar, J. E. Sevransky, C. L. Sprung, M. E. Nunnally, B. Rochweg, G. D. Rubenfeld, D. C. Angus, D. Annane, R. J. Beale, G. J. Bellingham, G. R. Bernard, J. D. Chiche, C. Coopersmith, D. P. De Backer, C. J. French, S. Fujishima, H. Gerlach, J. L. Hidalgo, S. M. Hollenberg, A. E. Jones, D. R. Karnad, R. M. Kleinpell, Y. Koh, T. C. Lisboa, F. R. Machado, J. J. Marini, J. C. Marshall, J. E. Mazuski, L. A. McIntyre, A. S. McLean, S. Mehta, R. P. Moreno, J. Myburgh, P. Navalesi, O. Nishida, T. M. Osborn, A. Perner, C. M. Plunkett, M. Ranieri, C. A. Schorr, M. A. Seckel, C. W. Seymour, L. Shieh, K. A. Shukri, S. Q. Simpson, M. Singer, B. T. Thompson, S. R. Townsend, T. Van der Poll, J. L. Vincent, W. J. Wiersinga, J. L. Zimmerman, R. P. Dellinger, *Intensive Care Med.* **2017**, *45*, 304.
- [8] J. Teboul, B. Saugel, M. Cecconi, D. De Backer, C. K. Hofer, X. Monnet, A. Perel, M. R. Pinsky, D. A. Reuter, A. Rhodes, P. Square, J. Vincent, T. W. Scherren, *Intensive Care Med.* **2016**, *42*, 1350.
- [9] S. T. Venkataraman, A. E. Thompson, R. A. Orr, *Clin. Pediatr.* **1997**, *36*, 311.
- [10] M. R. Miller, M. Griswold, J. M. Harris, G. Yenokan, W. C. Huskins, M. Moss, T. B. Rice, D. Ridling, D. Campbell, P. Margolis, S. Muething, R. J. Brilli, *Pediatrics* **2010**, *125*, 206.
- [11] A. A. DuMond, E. da Cruz, M. C. Almodovar, R. H. Friesen, *Pediatr. Crit. Care Med.* **2012**, *13*, 39.
- [12] N. Ilonzo, A. Rao, K. Soundararajan, A. Vouyouka, D. Han, R. Tadros, S. Y. Kim, B. Love, W. Ting, M. Marin, P. Faries, *J. Vasc. Surg.* **2020**, *72*, 403.
- [13] J. Phua, L. Weng, L. Ling, M. Egi, C. Lim, J. V. Divatia, B. R. Shrestha, Y. M. Arabi, J. Ng, C. D. Gomersall, M. Nishimura, Y. Koh, B. Du, *Lancet Respir. Med.* **2020**, *8*, 506.
- [14] S. Gerke, C. Shachar, P. R. Chai, I. G. Cohen, *Nat. Med.* **2020**, *26*, 1176.
- [15] J. A. Bielicki, X. Duval, N. Gobat, H. Goossens, M. Koomans, E. Tacconelli, *Lancet Infect. Dis.* **2020**, *20*, 261.
- [16] J. M. Black, J. E. Cuddigan, M. A. Walko, L. A. Didier, M. J. Lander, M. R. Kelp, *Int. Wound J.* **2010**, *7*, 358.
- [17] R. W. Morris, M. Nairn, M. Beaudoin, *Anaesth. Intensive Care Med.* **1990**, *18*, 107.
- [18] S. F. Baker, B. J. Smith, P. K. Donohue, C. A. Gleason, *J. Perinatol.* **1999**, *19*, 426.
- [19] M. M. Baharestani, C. R. Ratliff, *Adv. Skin Wound Care* **2007**, *20*, 208.
- [20] N. Anast, M. Olejniczak, J. Ingrande, J. Brock-Utne, *Can. J. Anaesth.* **2016**, *63*, 298.
- [21] H. U. Chung, A. Y. Rwei, A. Hourlier-Fargette, S. Xu, K. H. Lee, E. C. Dunne, Z. Xie, C. Liu, A. Carlini, D. H. Kim, D. Ryu, E. Kulikova, J. Cao, I. C. Odland, K. B. Fields, B. Hopkins, A. Banks, C. Ogle, D. Grande, J. B. Park, J. Kim, M. Irie, H. Jang, J. H. Lee, Y. Park, J. Kim, H. H. Jo, H. Hahm, R. Avila, Y. Xu, M. Namkoong, J. W. Kwak, E. Suen, M. A. Paulus, R. J. Kim, B. V. Parsons, K. A. Human, S. S. Kim, M. Patel, W. Reuther, H. S. Kim, S. H. Lee, J. D. Leedle, Y. Yun, S. Rigali, T. Son, I. Jung, H. Arafa, V. R. Soundararajan, A. Ollech, A. Shukla, A. Bradley, M. Schau, C. M. Rand, L. E. Marsillio, Z. L. Harris, Y. Huang, A. Hamvas, A. S. Paller, D. E. Weese-Mayer, J. Y. Lee, J. A. Rogers, *Nat. Med.* **2020**, *26*, 418.
- [22] F. S. Cattivelli, H. Garudadri, *IEEE 2009 Sixth Int. Workshop on BSN*, IEEE, Piscataway, NJ **2009**, p. 114.
- [23] R. Wang, W. Jia, Z. H. Mao, R. J. Scabassi, M. Sun, *IEEE 2014 12th Int. Conf. on Signal Processing (ICSP)*, IEEE, Piscataway, NJ **2014**, p. 115.
- [24] M. S. Dhillon, M. J. Banet, in *The Handbook of Cuffless Blood Pressure Monitoring: A Practical Guide for Clinicians, Researchers, and Engineers* (Eds: J. Sola, R. Delgado-Gonzalo), Springer, Switzerland **2019**, Ch. 5.
- [25] M. Banet, M. Dhillon, D. McCombie, (Sotera Wireless), *U.S. Patent 8602997*, **2013**.
- [26] J. Blaber, B. Adair, A. Antoniou, *Exp. Mech.* **2015**, *55*, 1105.
- [27] J. T. Kim, J. Nam, S. Shen, C. Lee, L. P. Chamorro, *J. Fluid Mech.* **2020**, *891*, A7.
- [28] V. Placet, P. Delobelle, *J. Micromech. Microeng.* **2015**, *25*, 035009.
- [29] R. Hopf, L. Bernardi, J. Menze, M. Zundel, E. Mazza, A. E. Ehret, *J. Mech. Behav. Biomed. Mater.* **2016**, *60*, 425.
- [30] I. D. Johnson, D. K. McCluskey, C. K. L. Tan, M. C. Tracey, *J. Micromech. Microeng.* **2014**, *24*, 035017.
- [31] A. C. M. Yang, *Polymer* **1994**, *35*, 3206.
- [32] M. Patel, A. R. Skinner, *Polym. Degrad. Stab.* **2001**, *73*, 399.
- [33] M. Patel, A. R. Skinner, R. S. Maxwell, *Polym. Test.* **2005**, *24*, 663.
- [34] J. Stein, L. C. Prutzman, *J. Appl. Polym. Sci.* **1988**, *36*, 511.
- [35] H. U. Chung, B. H. Kim, J. Y. Lee, J. Lee, Z. Xie, E. M. Ibler, K. Lee, A. Banks, J. Y. Jeong, J. Kim, C. Ogle, D. Grande, Y. Yu, H. Jang, P. Assem, D. Ryu, J. W. Kwak, M. Namkoong, J. B. Park, Y. Lee, D. H. Kim, A. Ryu, J. Jeong, K. You, B. Ji, Z. Liu, Q. Huo, X. Feng, Y. Deng, Y. Xu, K.-I. Jang, J. Kim, Y. Zhang, R. Ghaffari, C. M. Rand, M. Schau, A. Hamvas, D. E. Weese-Mayer, Y. Huang, S. M. Lee, C. H. Lee, N. R. Shanbhag, A. S. Paller, S. Xu, J. A. Rogers, *Science* **2019**, *363*, 0780.
- [36] R. M. Ryan, G. E. Wilding, R. J. Wynn, R. C. Welliver, B. A. Holm, C. L. Leach, *J. Perinatol.* **2011**, *31*, 607.
- [37] M. Buonanno, D. Welch, I. Shuryak, D. J. Brenner, *Sci. Rep.* **2020**, *10*, 10285.
- [38] M. Raeiszadeh, B. Adeli, *ACS Photonics* **2020**, *7*, 2941.
- [39] M. Biasin, A. Bianco, G. Pareschi, A. Cavalleri, C. Cavatorta, C. Fenizia, P. Galli, L. Lessio, M. Lualdi, E. Tombetti, A. Ambrosi, E. M. A. Redaelli, I. Saulle, D. Trabattoni, A. Zanutta, M. Clerici, *Sci. Rep.* **2021**, *11*, 1.
- [40] Z. W. Lipsky, G. K. German, *J. Mech. Behav. Biomed. Mater.* **2019**, *100*, 103391.
- [41] Z. Farhadinejad, M. Ehsani, I. Ahmadi-Joneidi, A. A. Shayegani, H. Mohseni, *IEEE Trans. Dielectr. Electr. Insul.* **2012**, *19*, 1740.
- [42] S. Valouch, H. Sieber, S. Kettlitz, *Opt. Express* **2012**, *20*, 28855.
- [43] M. Ouyang, C. Yuan, R. J. Muisener, A. Boulares, J. T. Koberstein, *Chem. Mater.* **2000**, *12*, 1591.
- [44] Y. Berdichevsky, J. Khandurina, A. Guttman, Y. H. Lo, *Sens. Actuators, B* **2004**, *97*, 402.
- [45] K. Efimenko, W. E. Wallace, J. Genzer, *J. Colloid Interface Sci.* **2002**, *254*, 306.
- [46] A. Mata, A. J. Fleischman, S. Roy, *Biomed. Microdevices* **2005**, *7*, 281.
- [47] S. S. Voyutskii, V. L. Vakula, *J. Appl. Polym. Sci.* **1963**, *7*, 475.
- [48] A. D. Zimon, *Adhesion of Dust and Powder*, Springer, New York, NY, USA **1982**.
- [49] M. E. Schrader, *Langmuir* **1995**, *11*, 3585.
- [50] J. Yang, R. Bai, B. Chen, Z. Suo, *Adv. Funct. Mater.* **2020**, *30*, 1901693.
- [51] K. Tian, J. Bae, Z. Suo, J. J. Vlassak, *ACS Appl. Mater. Interfaces* **2018**, *10*, 43252.
- [52] I. B. Wilkinson, H. MacCallum, L. Flint, J. R. Cockcroft, D. E. Newby, D. J. Webb, *J. Physiol.* **2000**, *525*, 263.
- [53] M. Sharma, K. Barbosa, V. Ho, D. Griggs, T. Ghirmai, S. K. Krishnan, T. K. Hsiai, J.-C. Chiao, H. Cao, *Technologies* **2017**, *5*, 21.
- [54] Y. Ma, J. Choi, A. Hourlier-Fargette, Y. Xue, H. U. Chung, J. Y. Lee, X. Wang, Z. Xie, D. Kang, H. Wang, S. Han, S.-K. Kang, Y. Kang, X. Yu, M. J. Slepian, M. S. Raj, J. B. Model, X. Feng, R. Ghaffari, J. A. Rogers, Y. Huang, *Proc. Natl. Acad. Sci. USA* **2018**, *115*, 11144.

- [55] W. J. Verberk, in *The Handbook of Cuffless Blood Pressure Monitoring: A Practical Guide for Clinicians, Researchers, and Engineers* (Eds: J. Sola, R. Delgado-Gonzalo), Springer, Switzerland **2019**, Ch. 12.
- [56] B. Campbell, *Heart Lung* **1997**, 26, 204.
- [57] W. B. White, A. S. Berson, C. Robbins, M. J. Jamieson, L. M. Prisant, E. Roccella, S. G. Sheps, *Hypertension* **1993**, 21, 504.
- [58] M. P. Kain, B. M. Bolker, M. W. McCoy, *PeerJ* **2015**, 3, 1226.
- [59] B. M. van Paridon, C. Sheppard, G. G. Guerra, A. R. Joffe, *Crit. Care* **2015**, 19, 293.
- [60] E. Mikluic, J. N. Cohn, J. A. Franciosa, *Circulation* **1977**, 56, 528.
- [61] M. Gao, N. B. Olivier, R. Mukkamala, *Physiol. Rep.* **2016**, 4, 12768.
- [62] P. P. Pandharipande, B. T. Pun, D. L. Herr, M. Maze, T. D. Girard, R. R. Miller, A. K. Shintani, J. L. Thompson, J. C. Jackson, S. A. Deppen, R. A. Stiles, R. S. Dittus, G. R. Bernard, E. W. Ely, *JAMA, J. Am. Med. Assoc.* **2007**, 298, 2644.
- [63] J. Barr, K. Zomorodi, E. J. Bertaccini, S. L. Shafer, E. Geller, *Anesthesiology* **2001**, 95, 286.
- [64] W. R. Martin, D. R. Jasinski, C. A. Haertzen, D. C. Kay, B. E. Jones, P. A. Mansky, R. W. Carpenter, *Arch. Gen. Psychiatry* **1973**, 28, 286.
- [65] S. Alinejad, T. Kazemi, N. Zamani, R. S. Hoffman, O. Mehrpour, *EX-CLI J.* **2015**, 14, 577.
- [66] S. Cunningham, S. Deere, N. McIntosh, *Arch. Dis. Child.* **1993**, 69, 64.
- [67] K. R. Dunster, P. B. Colditz, G. J. Joy, *Arch. Dis. Child. Fetal Neonatal Ed.* **1994**, 70, F77.
- [68] S. Cunningham, A. G. Symon, R. A. Elton, C. Zhu, N. McIntosh, *Early Hum. Dev.* **1999**, 56, 151.
- [69] R. G. Khemani, A. Randolph, B. Markovitz, *Cochrane Database Syst. Rev.* **2009**, 3, CD001000.
- [70] J. Jansaitong, *J. Spec. Pediatr. Nurs.* **2001**, 6, 182.
- [71] A. Ohlsson, S. A. Calvert, M. Hosking, A. T. Shennan, *Acta Paediatr.* **1992**, 81, 751.
- [72] B. Goldstein, M. H. Kempster, D. B. DeKing, C. Cox, D. J. DeLong, M. M. Kelly, P. D. Woolf, *Crit. Care Med.* **1996**, 24, 234.
- [73] D. Solav, M. B. Rubin, A. Cereatti, V. Camomilla, A. Wolf, *Ann. Biomed. Eng.* **2016**, 44, 1181.
- [74] Y. C. Kim, S. H. Kim, D. Kim, S. J. Park, J. K. Park, *Sens. Actuators, B* **2010**, 145, 861.